Published August 11, 2016

Original Research

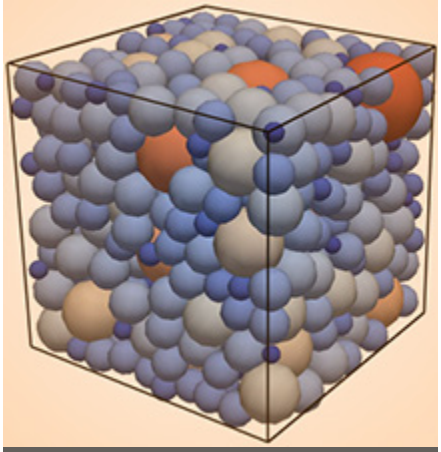

Effects of Sand Compaction and Mixing on Pore Structure and the Unsaturated Soil Hydraulic Properties

M.G. Mahmoodlu,* A. Raoof, T. Sweijen, and M. Th. van Genuchten

The hydraulic properties of unsaturated porous media very much depend on their pore structure as defined by the size, arrangement, and connectivity of pores. Several empirical and quasi-empirical approaches have been used over the years to derive pore structure information from the particle size distribution. In this study, we used the discrete element method to simulate the pore structure of various sands as affected by compaction and particle mixing processes. We used five sands with different mean grain sizes to investigate the effects of different sand mixing ratios and degrees of compaction on pore structure as well as on the intrinsic permeability and the soil water retention curve. Average pore body and pore throat sizes were found to be determined mostly by the smaller particles as represented by the effective diameter D_{10}. The effects of compaction on the average pore body and pore throat radii were used to simulate expected decreases in the permeability. We obtained mostly linear relationships between permeability and the average pore body and throat radii when mixing different unimodal sands. The intrinsic permeability of the coarser sands was found to be far more sensitive to porosity than the finer sands. Simulations of unsaturated conditions showed that the van Genuchten hydraulic parameter α increased nonlinearly with increasing grain size and mean pore body size of the sand mixtures. Compaction caused a linear decrease in α with decreasing porosity and pore body size. However, no clear correlation between the van Genuchten parameter n and porosity or D_{10} was found for the different compaction and mixing simulations.

Abbreviations: DEM, discrete element method; SWRC, soil water retention curve

Core Ideas

- A discrete element model was used to extract the pore structure of particle packings.
- Soil grain compaction and size mixing affect pore structure.
- Size mixing had a greater effect than compaction on the pore size distribution.
- Compaction caused the SWRCs to change uniformly with porosity.
- Compaction decreased the van Genuchten α parameter but had less effect on n.

M.G. Mahmoodlu, Dep. of Earth Sciences, Utrecht Univ., Utrecht, the Netherlands, and Dep. of Watershed and Rangeland Management, Gonbad Kavous Univ., Iran; A. Raoof and T. Sweijen, Dep. of Earth Sciences, Utrecht Univ., Utrecht, the Netherlands; M.Th. van Genuchten, Dep. of Earth Sciences, Utrecht Univ., Utrecht, the Netherlands, and Dep. of Mechanical Engineering, Federal University of Rio de Janeiro, Rio de Janeiro, RJ, Brazil. *Corresponding author (m.g.mahmoodlu@gmail.com).

Vadose Zone J.
doi:10.2136/vzj2015.10.0136
Supplemental material online.
Received 5 Oct. 2015.
Accepted 19 May 2016.

Vol. 15, Iss. 8, 2016

Temporal changes in the soil hydraulic properties due to compaction can affect a range of near-surface and subsurface flow processes. Several natural and human-induced processes such as the use of farm machinery in agricultural operations, grazing activities, raindrop impact, timber harvesting in forests, fire, and various geotechnical engineering projects can lead to soil compaction (e.g., Richard et al., 2001a, 2001b; Assouline, 2006a; Keller et al., 2013; Kuncoro et al., 2014). Soil compaction alters pore spaces and consequently affects the bulk density, porosity, and soil hydraulic properties. Many studies over the years have shown that soil compaction and related surface sealing problems at the field scale lead to reductions in (i) infiltration and recharge rates, (ii) soil aeration and the gas diffusivity, (iii) the efficiency of fertilizer use, (iv) seedling emergence, and (v) the growth and distribution of plant roots (e.g., Bradford et al., 1987; Richard et al., 2001a, 2001b; Hadas, 2004; Wall and Heiskanen, 2009; Glab and Kopec, 2009; Vahyala et al., 2013; Kuncoro et al., 2014; Gregorich et al., 2014; Masís-Meléndez et al., 2015; Berli et al., 2015; Sela et al., 2015). Compaction and the related processes of pore clogging and soil deformation were comprehensively reviewed by Assouline (2006a) and Keller et al. (2013).

Changes in the soil physical and hydraulic properties may also occur in the absence of compaction. For example, fine sediment infiltration can lead to the deposition of small-sized

sediments into relatively large near-surface soil pores, thus leading to low-permeability surface horizons (Cui et al., 2008; Evans and Wilcox, 2014) and reducing the rates of water flow into and through the soil profile (Haghnazari et al., 2015). On the other hand, reductions in water percolation due to fine sediment infiltration may be advantageous for certain hydraulic structures such as dam reservoirs and qanat tunnels, as well as promoting water harvesting in dry climates by increasing runoff.

Transport parameters determine flow and solute transport through the soil column (Mahmoodlu et al., 2014, 2015). Soil compaction and fine sediment infiltration tend to reduce the porosity, hydraulic conductivity, and soil water retention. Pore-scale studies are important to understand the basic processes causing these changes in the soil hydraulic properties. Most previous studies on soil compaction and pore structure have involved quasi-empirical approaches and the use of pedotransfer functions (e.g., Rawls et al., 1983; Rajkai et al., 1996) or expressing selected soil water retention parameters as a function of bulk density or porosity (e.g., Baumhardt et al., 1990; Assouline, 2006a). An overview of the more refined analytical and numerical modeling approaches related to soil deformation and compaction was provided by Keller et al. (2013).

Studies of compaction and grain mixing effects on the unsaturated soil hydraulic properties require precise studies of the geometry of sand grains and related pore structures in terms of the prevailing pore body and pore throat sizes. Although the soil particle size distribution is relatively easy to measure using a range of techniques (Gee and Or, 2002), estimation of grain positions and pore structures cannot be done in the same way (Mehlhorn et al., 2008). One direct method to measure pore structures is the use of X-ray microtomography, which can provide detailed three-dimensional images of the medium (e.g., Peth et al., 2010; Cnudde and Boone, 2013; Vaz et al., 2014). However, X-ray microtomography is still relatively expensive and can serve only as a first step for identifying the pore structure. Image processing is the next step to obtain pore structure geometries, which often requires further analysis (Mehlhorn et al., 2008).

An alternative method is to consider idealized grain geometries to obtain pore structures for a given particle size distribution (Mehlhorn et al., 2008; Keller et al., 2013). In this study, we used the discrete element method (DEM) to simulate the movement of grains and to obtain the resulting pore structures for a variety of packings. For this purpose, we used the open source platform Yade-DEM (Šmilauer et al., 2015), which also enables computation of the hydraulic properties as well as the soil water retention curve (SWRC). The specific objectives of this study were to: (i) use the discrete element model to extract pore structures of different particle packings; (ii) explore the effects of soil grain compaction and mixing on pore structures; (iii) investigate the effects of compaction and mixing on the intrinsic permeability; and (iv) evaluate the effects of compaction and mixing on the SWRCs, including the van Genuchten hydraulic parameters α and n. In our approach, we kept the grain size distribution constant while increasing the level of compaction, thus reducing the porosity value and increasing the bulk density. For the mixing simulations, on the other hand, we kept the total porosity constant while varying the particle size distribution.

Sand Properties and Packings

As input to the discrete element models, we used the particle size distributions of five filter sands (Fig. 1). The sands originated from a river bed in Papendrecht (the Netherlands) and were sieved to different retained sizes as given in Table 1. The mean particle size varied from 350 to 1300 μm (Table 1). X-ray fluorescence analyses showed that >96% of the sand grains consisted of silica (SiO_2). Microscopic images of the sands showed a good degree of roundness of the sand grains (Fig. 1), which is an advantage for using the DEM. Coefficients of uniformity and curvature, given by $C_u = D_{60}/D_{10}$ and $C_c = (D_{30})^2/(D_{10}D_{60})$, respectively, were estimated for all sands (Table 1). Because C_u was <4 for all sands, the samples can be considered to be uniformly graded by containing essentially identical particle sizes. Sand S2 was the most uniform (Fig. 1), and hence used as the main sand for mixing with the other samples. We considered the coefficient of curvature (C_c) as another useful measure of the shape of the particle size distribution curve. This coefficient is sometimes used to differentiate the degree of sorting of a soil. Sand S1 showed a lesser degree of sorting, as reflected in its bimodal grain size distribution (Fig. 1).

In view of its favorable C_u and C_c values, we used Sand S2 as the main sand for our study. We considered various combinations of S2 with the other sands, as shown in Fig. 2, to explore the effects of mixing. A total of 13 samples were considered: the five main

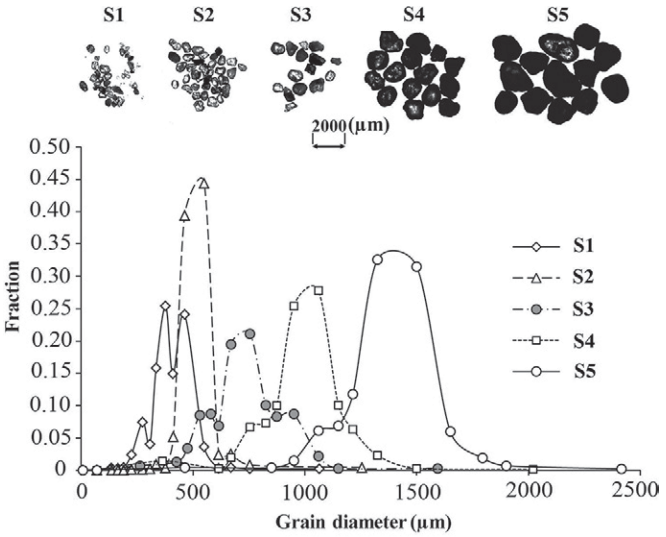

Fig. 1. Shape and diameter of the main sand particles (top) and their particle size distributions (bottom).

Table 1. The mean size, effective and mean diameters (D_{10} and D_{50}, respectively), coefficients of uniformity and curvature (C_u and C_c, respectively), pH, and total organic C (TOC) in dry samples of the natural sands used in this study.

Sand	Mean size	D_{10}	D_{50}	C_u	C_c	pH	TOC
	μm						g m^{-3}
S1	200–500	290	390	1.140	1.063	7	$<5.0 \times 10^{-20}$
S2	400–630	425	500	1.100	1.001		
S3	500–1000	540	710	1.187	0.983		
S4	700–1250	800	990	1.132	1.005		
S5	1000–1600	1140	1360	1.102	1.020		

sands (S1–S5; Table 1) and eight combinations of S2 with the other sands (Fig. 2). The porosities of all main sand samples were set at 0.40. The different sand grain combinations were used to calculate values of D_{10} (referred to as the effective diameter), D_{30} (the grain diameter corresponding to 30% w/w passing), D_{50} (median diameter), and D_{60} (the grain diameter corresponding to 60% w/w passing) of the mixtures. Figure 2 shows the calculated D_{10} and D_{50} values of the main sand (S2) and the various combinations. As expected, D_{10} and D_{50} both increased for the grain size distributions of the coarser sands and mixtures. We next used the particle size distributions of the different sands (Table 1) and their mixtures (Fig. 2) to extract their pore structures.

To observe the evolution of soil properties during compaction, we computed for each sample their pore structure geometries at five different porosities. Porosity values during compaction were assumed to decrease from 0.40 to 0.30 at intervals of 0.025. For each of the resulting porosities, we then calculated the pore structure, the SWRC, and the intrinsic permeability.

The Discrete Element Method

General Principles

Discrete element models are being used increasingly in soil and rock mechanics to explore deformation and shear strength properties of granular materials (Cundall and Strack, 1979; Scholtès et al., 2009; Scholtès and Donzé, 2012) as well as for agricultural and industrial applications such as soil tillage (Xu et al., 2002; Shmulevich et al., 2007) and particle flows in silos (Coetzee and Els, 2009). In the DEM, grain particles are considered as spheres defined by their radius, mass, momentum, and acceleration. A large number of spheres are typically used to represent a particular soil packing. The approach assumes that a spring-type behavior occurs at the contact between spheres. Discrete element models for this reason are often referred to as spring-dashpot models (Cundall and Strack, 1979). In our study, we used the Yade-DEM software to simulate packings of particles for varying target porosities having different particle size distributions.

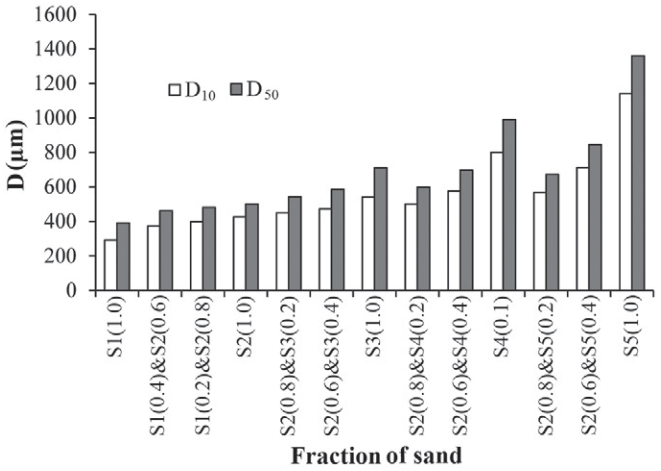

Fig. 2. The effective diameter (D_{10}) and mean diameter (D_{50}) of the different combinations of sand grains from sands S1 to S5.

We considered normal elasticity, tangential elasticity, and sliding as the main processes taking place at the contact points. Following a study by Labenne sand by Belheine et al. (2009), normal elasticity was calculated according to a linear contact law. When two particles are in contact and pushed toward each other by the surrounding medium, they are flattened at their contact point. The tendency of both particles to keep their initial shapes may cause an elastic force f_n:

$$f_n = k_n \delta_n \quad [1]$$

where k_n is a coefficient describing the stiffness of the particles and δ_n denotes the normal displacement.

As a result of the shear at the contact point, a tangential force, f_t, may arise. When the tangential force reaches a certain threshold value, the contact point will break, causing sliding of the two particles. This process is described by

$$f_t \leq f_n \tan\phi \quad [2]$$

where ϕ is the friction angle used to estimate the threshold value.

For each particle, a force balance is made by including forces due to contacts with other particles, the boundary conditions, and the effects of gravity. The resulting net force gives the acceleration of the particle, using Newton's second law. We refer to studies by Cundall and Strack (1979) and Belheine et al. (2009) for details.

Packing Simulations

The DEM was used to generate a packing of spherical particles for a certain porosity and particle size distribution. Initially, we selected 5000 particles from a given particle size distribution. These were inserted in a large box such that a cloud of particles was generated. The grain-scale parameters were taken from Belheine et al. (2009),

representing a dune sand. The values of particle stiffness, the friction angle, and Poisson's ratio were 9.6×10^8 Pa, 30.0°, and 0.04, respectively. All six boundaries of the domain were subsequently allowed to confine the particles until a porosity value of 0.45 was reached. After this point, only the top boundary was allowed to move down to further confine the particle packing until a target porosity was reached. From the resulting packing, the pore body and pore throat sizes were extracted using the pore unit method. Moreover, the resulting pore spaces were used to calculate the SWRC and the permeability. The final packing resulted in around 9500 pore throats and 11,500 pore units.

Calculation of Pore Structure

A regular triangulation method was used to extract the geometry of the pore structure (Chareyre et al., 2012; Yuan et al., 2015). In the application of this method, the pore space is divided into tetrahedrons, with each tetrahedron serving as a pore unit. As shown in Fig. 3, each tetrahedron is surrounding one pore body and has four vertices that are located at the centers of the spherical particles. The sides, or facets, of a tetrahedron are the locations at which two pore bodies are connected. The facet is the narrowest transect between two connecting pore units and is referred to as the *pore throat*. While some studies have suggested random pore connectivities due to the natural structure of porous media (Raoof and Hassanizadeh, 2010; Vasilyev et al., 2012; Li et al., 2014), our approach assumed that four pore throats are connected to each pore body. Each pore throat in this way is surrounded by three particles to which an inscribed circle can be fitted (Fig. 3c). The radius of this circle, R_{ij}, is taken as the pore throat radius (Torskaya et al., 2014). Inside a pore unit, an inscribed sphere exists that touches the four surrounding particles. The inscribed sphere is referred to as the *Haines insphere* (Gladkikh and Bryant, 2005; Unsal et al., 2009; Mousavi and Bryant, 2012; Prodanović et al., 2015), while its corresponding radius is denoted as R_i. Compaction was incorporated in the pore-scale calculations by repeated repacking and rearrangement of the spherical particles to decrease porosities to the prescribed values, with concomitant changes in the pore structures.

Calculation of Hydraulic Properties

The permeability of the granular material was computed using the pore finite volume method as implemented in the DEM by Chareyre et al. (2012). This method allows solving for the pressure distribution under fully water-saturated conditions. The approach assumes that one pressure value can be associated with each pore unit. The flux, q_{ij} [L^3 T^{-1}], of water from the ith pore unit to the jth pore unit is given by (Vasilyev et al., 2012)

$$q_{ij} = k_{ij} \frac{p_i - p_j}{l_{ij}} \quad [3]$$

where p_i and p_j [M L^{-1} T^{-2}] are the pressures in the ith and jth pore units, respectively, l_{ij} [L] is the length between the centers of the ith and jth pore units, and k_{ij} [M^{-1} L^5 T] denotes the hydraulic conductivity of the facet (pore throat) between the ith and jth pores, given by

$$k_{ij} = \frac{A_{ij}^f R_{ij}^2}{2\mu} \quad [4]$$

where A_{ij}^f [L^2] is the smallest transect of the pore throat, μ [M L^{-1}] is the dynamic viscosity, and R_{ij} [L] is the hydraulic radius of the facet:

$$R_{ij} = \frac{\Theta_{ij}}{\omega_{ij}} \quad [5]$$

where Θ_{ij} [L^3] is the pore throat volume and ω_{ij} [L^2] the surface of the pore throat. See Chareyre et al. (2012) for more details.

Under steady-state conditions, and assuming incompressible flow, the continuity equation provides that (Zhang et al., 2015)

$$\sum_{j=1}^{4} q_{ij} = 0 \quad [6]$$

Equations [3], [4], and [6] were solved implicitly to calculate pressure values (Raoof et al., 2010). The total flux through the medium was subsequently used to compute the permeability of the medium.

Capillary Pressure–Saturation Calculations

To estimate the capillary pressure–saturation (soil water retention) curve, the bottom boundary of the simulated domain was assumed to be a water reservoir at a fixed pressure, P_w, whereas the top boundary was considered to be an air reservoir with pressure P_{air}. Under quasi-static conditions, the capillary pressure, P_c, is then equal to the pressure difference between the two reservoirs:

$$P_c = P_{air} - P_w \quad [7]$$

For drainage (i.e., drying) simulations, the non-wetting air pressure was increased in steps to allow air to invade increasingly smaller pore throats. If the capillary pressure is larger than the entry pressure of a pore throat, air could invade a water-saturated pore unit. The entry pressure (P_e) of a pore throat can be obtained using the Young–Laplace equation:

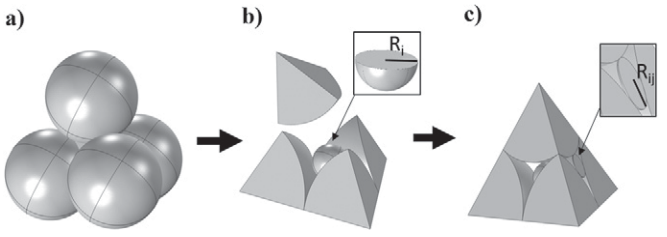

Fig. 3. Schematic of the (a) spherical packing with (b) a pore body with radius R_i and (c) a pore throat with radius R_{ij} as used in this study.

$$P_e = \frac{2\gamma}{R_{ij}} \quad [8]$$

where γ is the surface tension [M L^{-1} T^{-1}] and R_{ij} is the radius of the inscribed circle in the pore throat (Fig. 3c). During imbibition, the capillary pressure must be lower than the entry pressure before water may invade an air-saturated pore unit (Zhang et al., 2013). At each pressure step, the equilibrium positions of the air–water interfaces within the network are determined. From this information we can calculate the average saturation of the network at any given capillary pressure (e.g., Øren et al., 1998; Raoof and Hassanizadeh, 2012; Raoof et al., 2013).

To obtain the SWRC, the simulation procedure was as follows. After selecting a capillary pressure, we determined if a water-saturated pore unit could be invaded by a neighboring air-saturated pore unit. Both pore units had to be connected to their corresponding reservoir for invasion to occur. Disconnected water-saturated pores were used to calculate the irreducible (i.e., residual) water saturations. An algorithm was further implemented to keep track of disconnected air and water regions to ensure that no displacement of the disconnected pores could occur. See Sweijen et al. (2016) for more details.

Effect of Compaction and Mixing on Pore Structures

Pore Body Radius

We investigated changes in the pore body radius distribution due to the compaction and sand mixing processes. Figure 4 shows changes in the cumulative frequency distributions of the pore body radii for Sands S2 and S5 and their mixtures. Results for the other sands and mixtures are shown in Supplemental Fig. S1. The plots indicate that particle mixing significantly affects the pore-size distribution while the effects of compaction are far less substantial. Compaction caused a decrease in the porosity and, compared with mixing, caused a more uniform change in the pore space (Fig. 4a and 4b). This is consistent with previous experimental and modeling studies on the effects of compaction on pore structure (e.g., Matthews et al., 2010; Koch et al., 2011; Kuncoro et al., 2014). Moreover, an increase in the degree of compaction reduced the pore body radius and consequently the volume of pores. This causes a reduction in the volume of macropores as a fraction of the total volume of the soil medium (Koch et al., 2011; Kuncoro et al., 2014). Mixing Sand S2 with larger sand grains (i.e., Sands S3, S4, and S5) created mixtures with much larger pore body radii (Fig. 4c; Supplemental Fig. S1).

Pore Throat Radius

Fluid flow and capillary displacement processes in porous media are strongly affected by pore throat sizes because they provide constrictions along the flow paths. Figure 5 depicts the cumulative

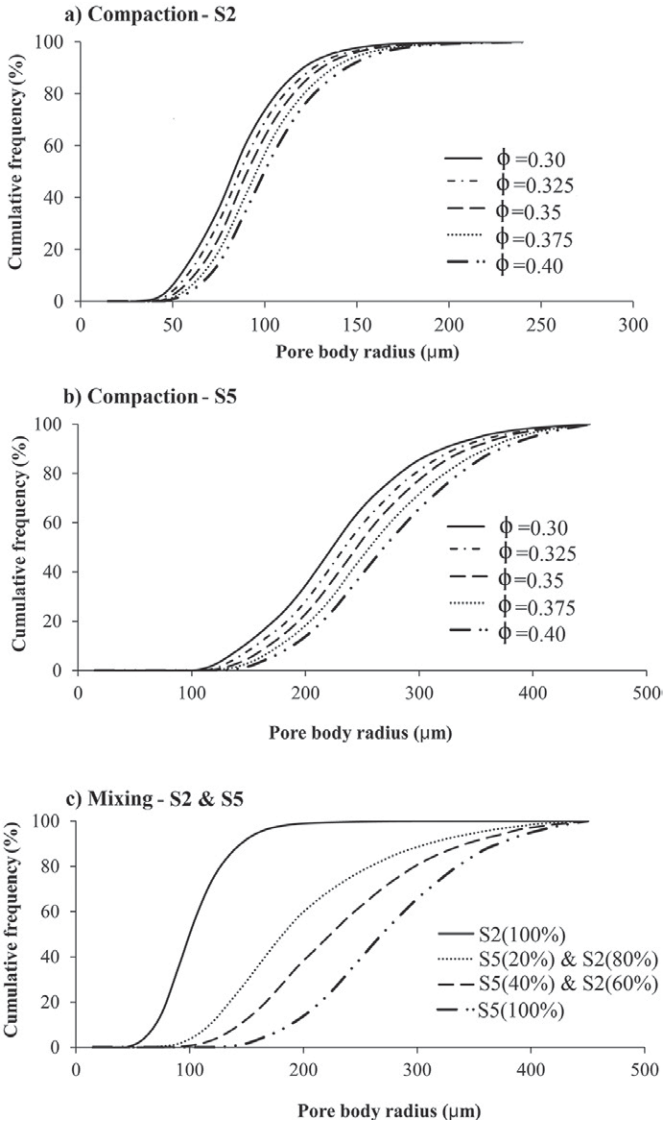

Fig. 4. Cumulative pore body radii distributions as affected by soil compaction (different porosities) of sands (a) S2 and (b) S5 and (c) as obtained by mixing different proportions of sands S2 and S5 for a porosity ϕ of 0.40.

frequency distributions of the pore throat radius obtained with the compaction and particle mixing simulations, again for Sands S2 and S5 and several of their mixtures. These results, as well as those for the other sands shown in Supplemental Fig. S2, show that the pore throat radii increase with increasing grain sizes, as expected. The simulations revealed a relatively uniform change in the pore throat radii of the sands during compaction, whereas the shapes of the pore throat radius distribution curves changed far less uniformly for the mixed samples. Because SWRCs are dominated by pore throat radii, at least in the wet range, one may expect uniform changes in the SWRC of each sand during the compaction process but more non-uniform changes as a consequence of mixing.

Mixing our main sand, S2, with larger grains created distributions with larger pore throats (Fig. 5c). Linear relationships were

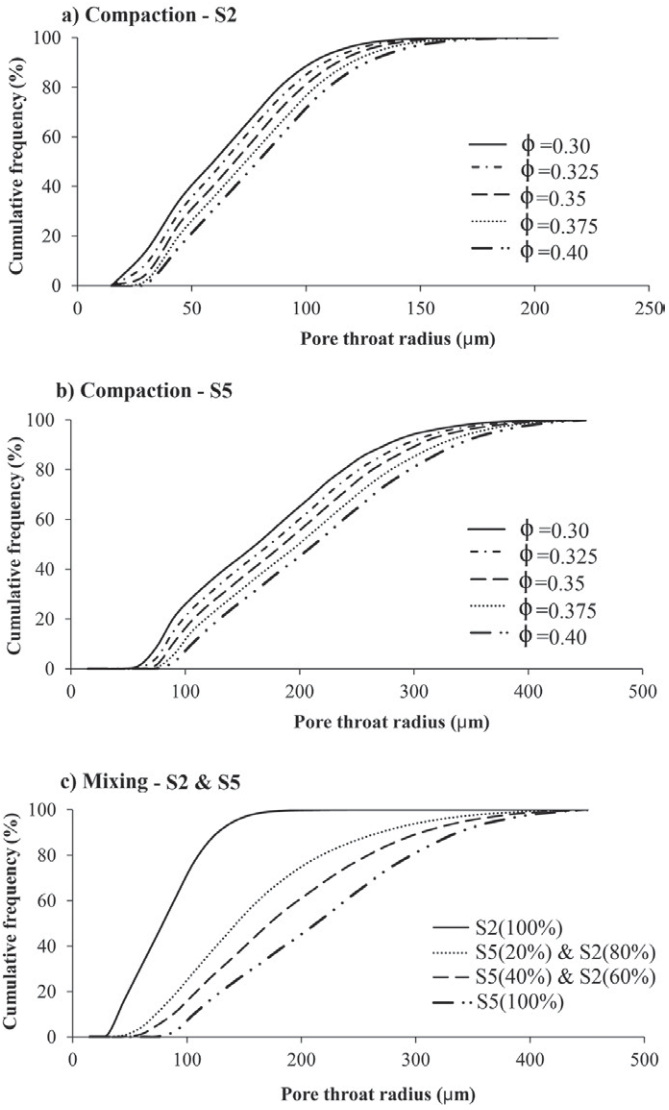

Fig. 5. Cumulative pore throat radii distributions as affected by soil compaction (different porosities) of sands (a) S2 and (b) S5 and (c) as obtained by mixing different proportions of sands S2 and S5 for a porosity ϕ of 0.40.

obtained between the average pore throat and pore body radii during both compaction and mixing (Supplemental Fig. S3).

Effect of Grain Diameter on Pore Body and Body Throat Radii

To investigate the effect of particle diameter on pore size during mixing of the sands, the average pore body and pore throat radii of all sands were calculated and plotted vs. D_{50} values (Fig. 6). The overall linear correlation indicates that the average pore body and throat size can be approximately estimated at a given porosity value. These types of correlations can be used to advantage to generate pore network models of soils with known porosity values.

We also investigated the effect of particle diameter on the pore body and pore throat radii. This was done by plotting the average pore body and pore throat radii as a function of the various particle

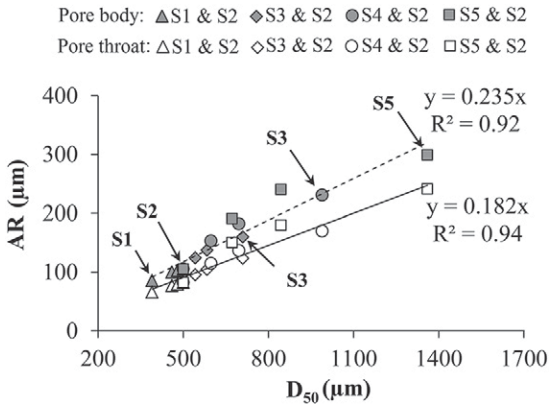

Fig. 6. Effect of the mean diameter (D_{50}, expressed as the soil particle size) of sands S1 to S5 and their mixtures on the average pore body and pore throat radii; AR is the average radius. For all mixtures, porosity was assumed to be 0.40.

diameters of the sand mixtures and then estimating the slopes of the fitted lines, such as for D_{50} in Fig. 6. We did the same for other soil particle D values (i.e., for D_{10}, D_{30}, and D_{60}). Our calculations showed that the slopes of the fitted lines were much higher for D_{10} than D_{50} and D_{60} (results not further shown here). This indicates that small soil grains are far more effective in changing the average pore body size, and hence that the average pore size is affected mostly by changes in the D_{10} value of a soil. In other words, the radii of relatively large pore bodies and pore throats are controlled mostly by the smaller soil grains.

We similarly plotted the average pore body and pore throat radii vs. D_{50} of the different mixtures of S2 with the other sands (Supplemental Fig. S4). A comparison of four graphs showed that the relationship between the average pore body and/or throat radius and D_{50} will be linear if the difference between the mean grain sizes of two main sands is very small (e.g., for S1 and S2). However, as shown in Supplemental Fig. S4, the relationships became nonlinear when differences between the mean grain sizes of the sands were more substantial, such as when mixing S2 and S5.

Evolution of Porosity and the Intrinsic Permeability

We next present DEM simulation results showing the effects of compaction and particle mixing on the pore body and pore throat radii and the intrinsic permeability. Figure 7 depicts changes in the average pore body and pore throat radii as a function of porosity. The average pore radii were found to increase linearly with porosity. Changes in porosity had more effect on the radii for the coarser sands, as indicated by the slightly steeper slopes in Fig. 7 especially for Sands S4 and S5. The plots in Fig. 7 demonstrate that different sand samples can have different average pore sizes at a given value of porosity.

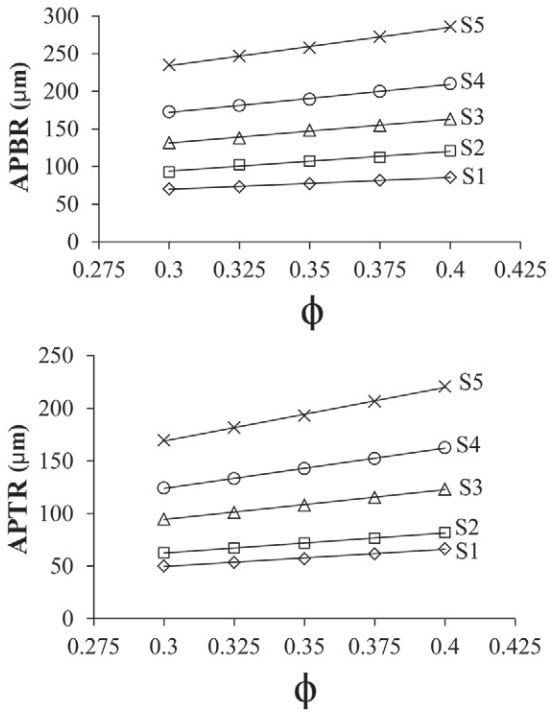

Fig. 7. Effect of porosity on the average pore body radius (APBR) and the average pore throat radius (APTR) of the different sand grain compactions (expressed as the porosity ϕ) of sands S1 to S5. The R^2 values of the regression were all between 0.99 and 1.00.

Results for the intrinsic permeability, *k*, are shown in Fig. 8. Soil permeability is determined by both the bulk geometric properties of a sample (e.g., porosity and the pore-size distribution) and topological properties such as pore space connectivity and tortuosity. The effect of the pore structure on the permeability was studied by mixing different fractions of the main sand (S2) with two other sand samples (S1 and S3). The results in Fig. 8a show that mixing the fine sand (S1) with S2 caused a steady reduction in the permeability, while mixing the coarser sand (S3) with S2 increased the permeability. This confirms that the permeability is mostly strongly affected by the larger pores (Håkansson and Lipiec, 2000; Assouline, 2006b). Mixing S2 with S3 hence causes an increase in the fraction of smaller pores of the coarser sand (here S3) and consequently a reduction in the permeability of Sand S3. By contrast, the permeability of S2 increased due to an increase in the fraction of larger pores. Our results clearly show that the permeability reductions of the coarser sand are dominated strongly by the relative amounts of the finer sands.

Table 2 compares calculated values of the intrinsic permeability with measured experimental values for Sands S1 and S2, as well as for their mixtures. While the measurements and simulation results both showed permeability reductions toward the finer sand, the simulated values for intrinsic permeability were much higher than the experimental values. The differences may be due to the fact that the pore finite volume method used in our study solves the flow problem locally at a very small scale and not at the

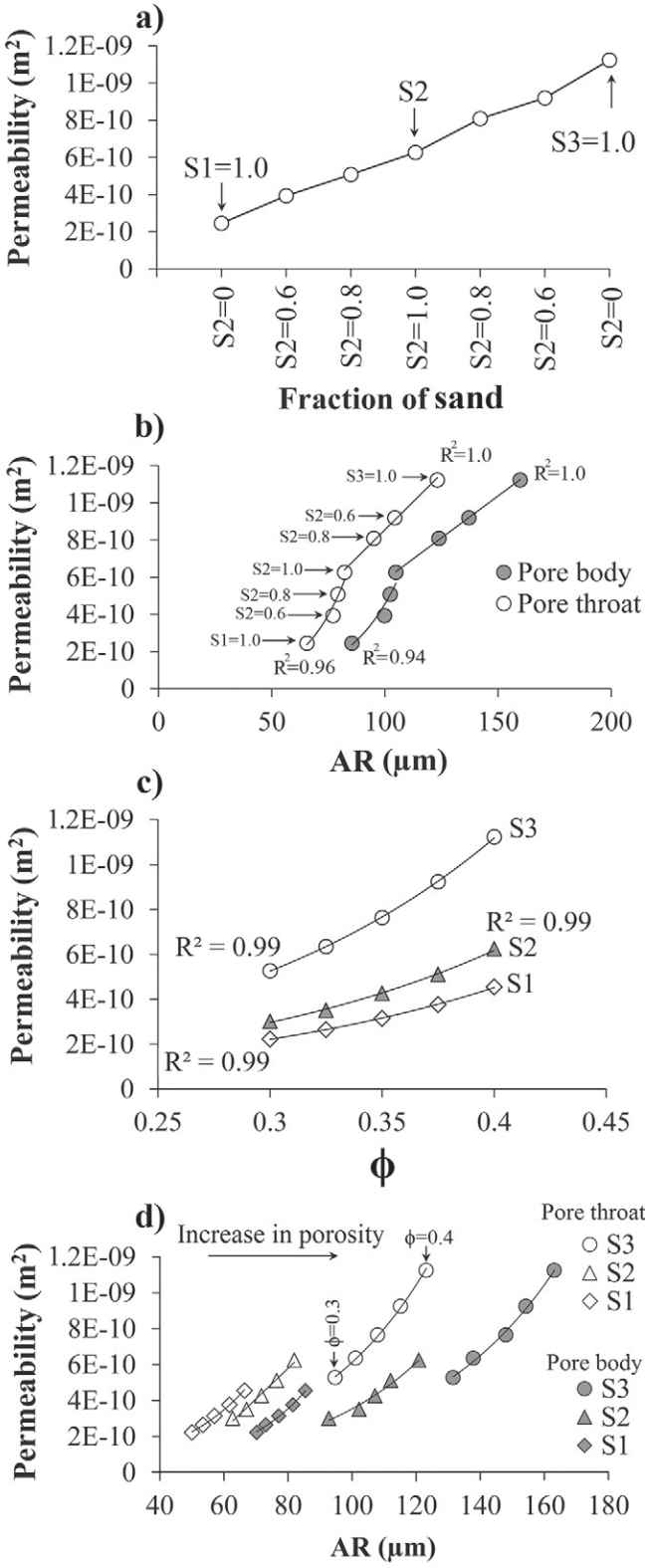

Fig. 8. Effect of sand grain mixing and compaction on the intrinsic permeability, *k*: (a) effect of mixing on *k* for three sands (S1, S2, and S3) and their mixtures for a porosity ϕ of 0.40; (b) relationship between pore body and throat radii and *k* for different sand grain mixtures; (c) effect of compaction (porosity) on *k* for three sands (S1, S2, and S3); and (d) values of *k* vs. pore body and throat radii for different porosities (porosities of the sands ranged from 0.3 on the left side of each curve to 0.4 on the right sides); AR is the average radius.

macroscopic level. This has been noted also by Tong et al. (2012), who, in a study of the effects of mixing on the permeability of glass beads, found similar differences between their experimental data and DEM simulations. Another possible reason may be the assumption in the DEM that the particles have a perfect spherical shape. Clearly, more studies on formulations of the DEM are needed to resolve the discrepancy between calculated and measured permeabilities.

Figure 8b shows that the relation between permeability and pore size became slightly nonlinear for the various mixtures of S1 and S2, while a more linear relationship was obtained for the mixtures of S2 and S3. We attribute this to the fact that Sand S1 had a more bimodal grain size distribution (Fig. 1), while S3 had a very regular (unimodal) grain size distribution (Fig. 1). The relationships between permeability and pore size were even more nonlinear when the permeability for a given porosity was plotted as a function of either the pore body radius or pore throat radius, as shown by the results in Fig. 8d.

We also evaluated the effects of compaction on calculated permeability values. For this, we used three sands (S1, S2, and S3) and calculated the intrinsic permeability at different porosity values (i.e., ϕ = 0.3, 0.325, 0.35, 0.375, and 0.4). Figure 8c indicates an exponential decrease in permeability as a function of porosity following compaction. The results showed that the changes in permeability are consistent with the changes in pore body and throat radii during compaction (Fig. 7). As explained above, the fraction of larger pores decreased when the samples were compacted. Figure 7 clearly shows that the pore body and throat radii, and hence the pore volumes, diminished with increased compaction. This may explain the reductions in permeability with compaction. Results also indicate that, in terms of absolute values, the permeability during compaction changed more for the coarser materials that the fine-textured sands (Fig. 8c).

Soil Water Retention Curve

Finally, we present DEM simulation results showing the effects of compaction and particle mixing on the SWRC. This curve has a first-order effect on predictions of water flow in variably saturated media. We investigated the effect of both pore body and pore throat size on the SWRC. Figure 9 shows the evolution of the volumetric water content, θ^w, as a function of capillary pressure, P_c, for some of the compaction and mixing simulations. Figures 9a and 9b indicate how saturated water contents decreased by diminishing the porosity due to the compaction. Also, however, at a given water content away from saturation, the capillary pressure was always higher for the more compacted samples due to the creation of smaller pore throats, which regulate higher capillary entry pressures and control capillary displacement (Supplemental Fig. S5). These findings are consistent with previous studies by Richard et al. (2001a), Assouline (2006a), and Matthews et al. (2010), among others, showing the effect of soil compaction on the SWRC.

Table 2. Comparison between experimental data and simulation results for the intrinsic permeability.

Sand	Intrinsic permeability	
	Simulation	Experiment
	$\times 10^{-11}$ m^2	
100% S1	24.5	6.4
40% S1, 60% S2	39.3	7.9
20% S1, 80% S2	50.8	8.6
100% S2	62.6	9.1

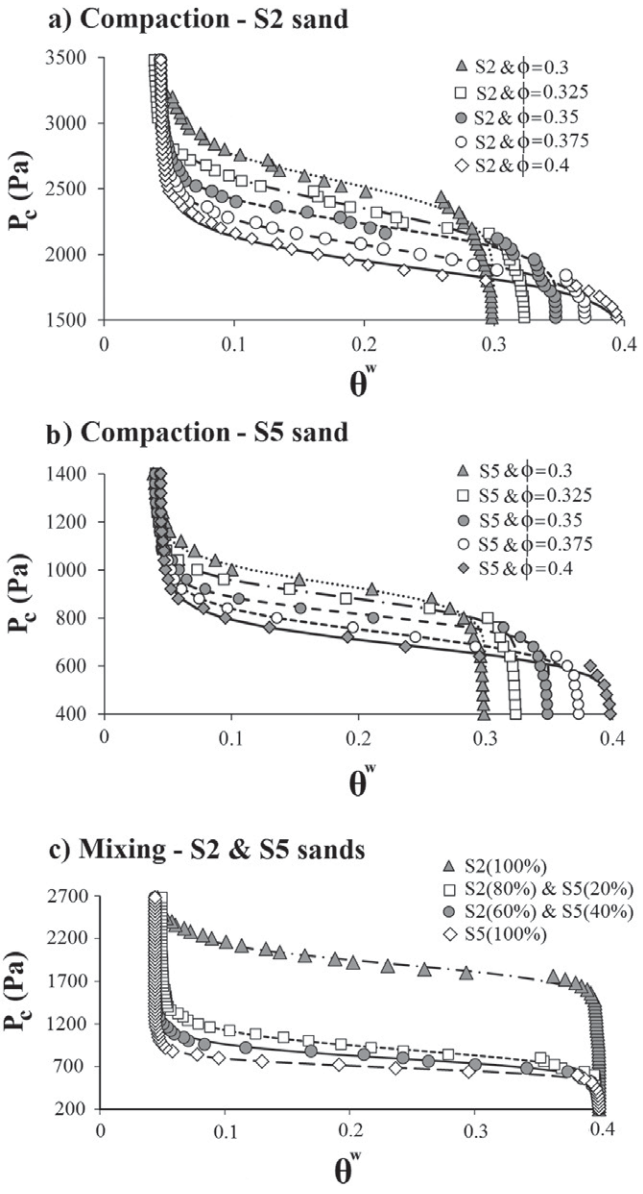

Fig. 9. Effect of compaction on the water retention curves of sands (a) S2 and (b) S5 and (c) of mixing different proportions of S2 and S5 on the soil water retention curve for a porosity ϕ of 0.40.

The simulated soil water retention curves were analyzed in terms of the water retention equation of van Genuchten (1980):

$$\theta^{w}(p_c) = \theta_r^{w} + \frac{\theta_s^{w} - \theta_r^{w}}{\left[1 + \left(\alpha |p_c|\right)^{n}\right]^{1-1/n}} \qquad p_c < 0 \qquad [9]$$

where θ^w (dimensionless) is the volumetric water content, θ_r^w (dimensionless) is the residual water content, θ_s^w (dimensionless) is the saturated water content, α [M^{-1} L T^2] and n (dimensionless) are shape parameters, and p_c [M L^{-1} T^{-2}] is the capillary pressure. Equation [9] was fitted to the SWRC data using the RETC code (van Genuchten et al., 1991). Results show that a decrease in porosity due to compaction leads to lower values of α (Fig. 10a). Figure 10b shows that an essentially linear relationship between the van Genuchten parameter α and the average pore throat radius (APTR) was obtained. This is not surprising because the pore throat size has a controlling effect on the entry pressure of pores. However, as opposed to a clear effect of compaction on the average pore throat radius, and hence on α, we did not find any noticeable effect of compaction on the van Genuchten parameter n. Supplemental Fig. S6 shows that n had little or no correlation with porosity (Supplemental Fig. S6). This should be expected because compaction, as modeled using the DEM, does not materially change the particle-size distribution, while the relative width (or normalized variance) of the pore-size distribution will remain very similar except for a shift in the distribution toward smaller pore sizes (and hence smaller values of the van Genuchten parameter α), at least for non-macroporous soils as considered in this study. These conclusions are very much consistent with several earlier experimental studies using repacked soils (e.g., Richard et al., 2001b; Stange and Horn, 2005).

For the mixing simulations, combining Sand S2 with a coarser sand caused a decrease in the capillary pressure at a given volumetric water content, and hence larger values of the α parameter. As shown in Fig. 10c, the van Genuchten parameter α increased nonlinearly with D_{50} expressed as the sand grain size. This was again expected because coarser soils are known to have larger α values (e.g., Carsel and Parrish, 1988). Similar to the compaction simulations, however, no clear correlation between the van Genuchten parameter n and sand grain size was found with the sand mixing simulations (Supplemental Fig. S6).

Finally, Fig. 10d shows that the SWRCs of all combinations of Sand S2 with the other sands changed non-uniformly with the APTR, except possibly for the mixture of S2 and S3. Moreover, mixing different fractions of S1 with S2 had only a relatively small effect on the SWRCs. This was due to minor changes in the pore throat radii of the mixtures compared with the main sand (S2).

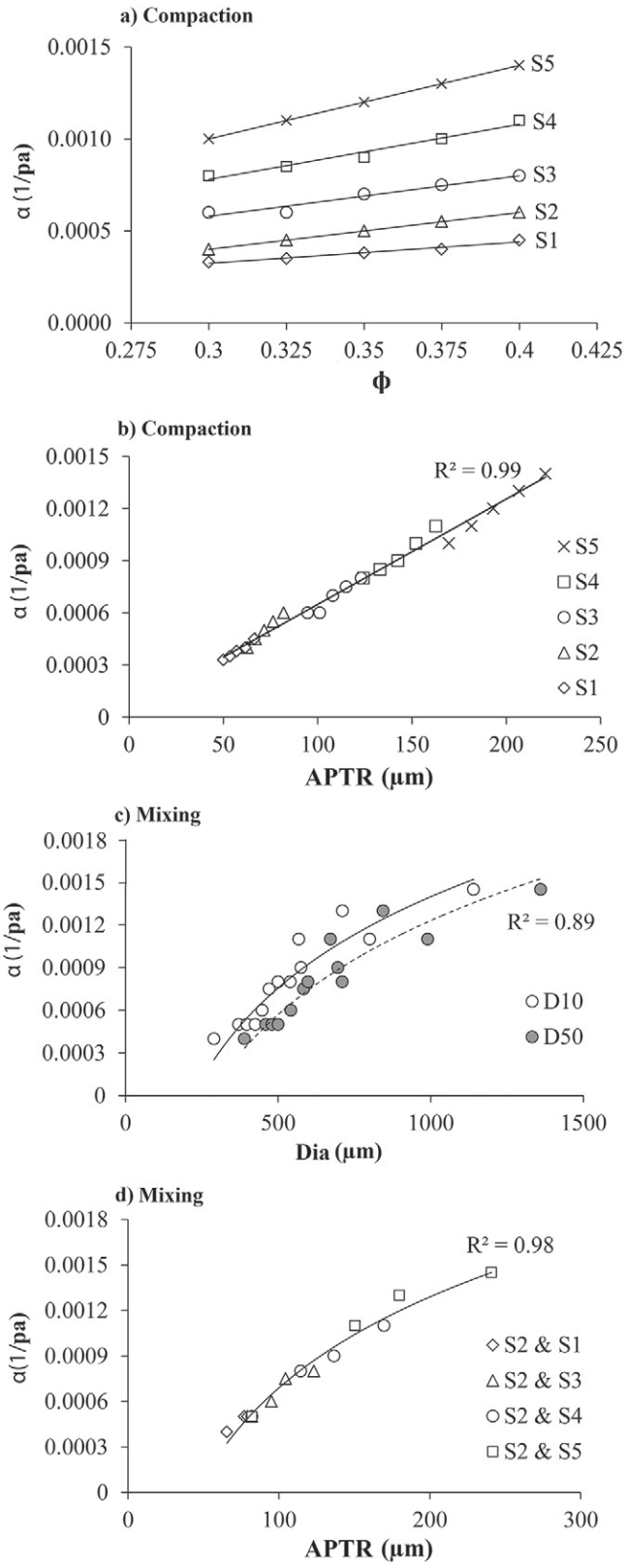

Fig. 10. Effect of different degrees of compaction and mixing of sands S1 to S5 in different combinations on the van Genuchten parameter α. Calculations for the mixing scenarios assumed a porosity ϕ of 0.40. The APTR is the average pore throat radius and Dia is the characteristic grain diameter (effective diameter D_{10} or mean diameter D_{50}).

Conclusions

In this study, we used five different sands (S1–S5) to investigate the effects of compaction as well as mixing of different sand types

on pore structure, intrinsic permeability, and the SWRC using coupled discrete element and pore-scale network modeling. We found that the average pore body and pore throat radii increased linearly with the median particle size (defined as D_{50}). Results for the various sand compaction and mixing scenarios showed that the effects of sand mixing on the pore-size distribution was far more important than compaction as such.

The results revealed that mixing with finer sands caused a reduction in the intrinsic permeability, while mixing with coarser sand increased the permeability of the mixture. We found that the relationship between permeability and pore size is affected by the type of grain size distribution—unimodal or bimodal. Mixing the unimodal sand, S2, with the bimodal sand, S1, caused a nonlinear relationship between permeability and pore body and throat radii, while mixing with other sands having a unimodal grain-size distribution produced linear relationships between permeability and pore body and throat radii.

An exponential increase in permeability with porosity was found, with permeability increasing much faster with porosity for the coarser sands. Our results showed that permeability increased nonlinearly with both pore body and throat radii. As expected, the saturated water content decreased with diminishing porosity under compaction. As opposed to the mixing simulations, compaction caused the SWRCs to change uniformly with porosity. The decrease in porosity, and hence the increase in bulk density, due to compaction caused smaller values of the van Genuchten parameter α. Values of α further decreased nonlinearly with decreasing sand D_{50} expressed as the sand grain size. No clear relationship between the van Genuchten parameter n and sand grain size was found.

The results of this study help to better understand the effects of sand mixing and compaction on soil pore structure and macroscopic soil hydraulic properties such as porosity, permeability, and soil water retention processes. This provides confidence that the pore-scale approach used here can be used ultimately to develop correlation relationships for use in field-scale models that account for soil compaction and mixing.

Acknowledgments

We would like to thank Filcom Company (Papendrecht, the Netherlands; www.filcom.nl) for supplying the sands and Hamed Aslannejad for taking microscopic images of sands. Comments by two anonymous referees and the VZJ Associate Editor further helped to improve the manuscript. This work is part of the Veni Research Program with Project no. 016.151.047, which is financed by the Netherlands Organization for Scientific Research (NWO).

References

Assouline, S. 2006a. Modeling the relationship between soil bulk density and the water retention curve. Vadose Zone J. 5:554–563. doi:10.2136/vzj2005.0083

Assouline, S. 2006b. Modeling the relationship between soil bulk density and the hydraulic conductivity function. Vadose Zone J. 5:697–705. doi:10.2136/vzj2005.0084

Baumhardt, R.L., M.J.M. Römkens, F.D. Whisler, and J.-Y. Parlange. 1990. Modeling infiltration into a sealing soil. Water Resour. Res. 26:2497–2505. doi:10.1029/WR026i010p02497

Belheine, N., J.P. Plassiard, F.V. Donzé, F. Darve, and A. Seridi. 2009. Numerical simulation of drained triaxial test using 3D discrete element modeling. Comput. Geosci. 36:320–331.

Berli, M., F. Casini, W. Attinger, R. Schulin, S.M. Springman, and J.M. Kirby. 2015. Compressibility of undisturbed silt loam soil: Measurements and simulations. Vadose Zone J. 14(8). doi:10.2136/vzj2014.10.0153

Bradford, J.M., J.E. Ferris, and P.A. Remley. 1987. Interrill soil erosion processes: I. Effect of surface sealing on infiltration, runoff, and soil splash detachment. Soil Sci. Soc. Am. J. 51:1566–1571. doi:10.2136/sssaj1987.03615995005100060029x

Carsel, R.F., and R.S. Parrish. 1988. Developing joint probability distributions of soil water retention characteristics. Water Resour. Res. 24:755–769. doi:10.1029/WR024i005p00755

Chareyre, B., A. Cortis, E. Catalano, and E. Barthélemy. 2012. Pore-scale modeling of viscous flow and induced forces in dense sphere packings. Transp. Porous Media 94:595–615. doi:10.1007/s11242-012-0057-2

Cnudde, V., and M.N. Boone. 2013. High-resolution X-ray computed tomography in geosciences: A review of the current technology and applications. Earth Sci. Rev. 123:1–17. doi:10.1016/j.earscirev.2013.04.003

Coetzee, C.J., and D.N.J. Els. 2009. Calibration of discrete element parameters and the modelling of silo discharge and bucket filling. Comput. Electron. Agric. 65:198–212. doi:10.1016/j.compag.2008.10.002

Cui, Y., J. Wooster, P. Baker, S. Dusterhoff, L. Sklar, and W. Dietrich. 2008. Theory of fine sediment infiltration into immobile gravel bed. J. Hydraul. Eng. 134:1421–1429. doi:10.1061/(ASCE)0733-9429(2008)134:10(1421)

Cundall, P.A., and O.D.L. Strack. 1979. A discrete numerical model for granular assemblies. Geotechnique 29:47–65. doi:10.1680/geot.1979.29.1.47

Evans, E., and A.C. Wilcox. 2014. Fine sediment infiltration dynamics in a gravel-bed river following a sediment pulse. River Res. Appl. 30:372–384. doi:10.1002/rra.2647

Gee, G., and D. Or. 2002. Particle size analysis. In: J.H. Dane and G.C. Topp, editors, Methods of soil analysis. Part 4. Physical methods. SSSA Book Ser. 5. SSSA, Madison, WI. p. 255–294. doi:10.2136/sssabookser5.4.c12

Glab, T., and S. Kopec. 2009. Effect of soil compaction on root system morphology and yields of meadow fescue (*Festuca pratensis*). Pol. J. Environ. Stud. 18:219–225.

Gladkikh, M., and S. Bryant. 2005. Prediction of imbibition in unconsolidated granular materials. J. Colloid Interface Sci. 288:526–539. doi:10.1016/j.jcis.2005.03.029

Gregorich, E.G., N.B. McLaughlin, D.R. Lapen, and P. Rochette. 2014. Soil compaction, both an environmental and agronomic culprit: Increased nitrous oxide emissions and reduced plant nitrogen uptake. Soil Sci. Soc. Am. J. 78:1913–1923. doi:10.2136/sssaj2014.03.0117

Hadas, A. 2004. Seedbed preparation: The soil physical environment of germination seeds. In: R.L. Benech-Arnold and R.A. Sanchez, editors, Handbook of seed physiology: Applications to agriculture. Hayworth Press, New York. p. 3–49.

Haghnazari, F., H. Shahgholi, and M. Feizi. 2015. Review: Factors affecting the infiltration of agricultural soils. Int. J. Agron. Agric. Res. 6(5):21–35.

Håkansson, I., and J. Lipiec. 2000. A review of the usefulness of relative bulk density values in studies of soil structure and compaction. Soil Tillage Res. 53:71–85. doi:10.1016/S0167-1987(99)00095-1

Keller, T., M. Lamande, S. Peth, M. Berli, J.-Y. Delenne, W. Baumgarten, et al. 2013. An interdisciplinary approach towards improved understanding of soil deformation during compaction. Soil Tillage Res. 128:61–80. doi:10.1016/j.still.2012.10.004

Koch, K., A. Kemna, J. Irving, and K. Holliger. 2011. Impact of changes in grain size and pore space on the hydraulic conductivity and spectral induced polarization response of sand. Hydrol. Earth Syst. Sci. 15:1785–1794. doi:10.5194/hess-15-1785-2011

Kuncoro, P.H., K. Koga, N. Satta, and Y. Muto. 2014. A study on the effect of compaction on transport properties of soil gas and water: I. Relative gas diffusivity, air permeability, and saturated hydraulic conductivity. Soil Tillage Res. 143:172–179. doi:10.1016/j.still.2014.02.006

Li, S., A. Raoof, and R. Schotting. 2014. Solute dispersion under electric and pressure driven flows: Pore scale processes. J. Hydrol. 517:1107–1113. doi:10.1016/j.jhydrol.2014.06.049

Mahmoodlu, M.G., S.M. Hassanizadeh, N. Hartog, and A. Raoof. 2014. Oxidation of trichloroethylene, toluene, and ethanol vapors by a partially saturated permeable reactive barrier. J. Contam. Hydrol. 164:193–208. doi:10.1016/j.jconhyd.2014.05.013

Mahmoodlu, M.G., S.M. Hassanizadeh, N. Hartog, A. Raoof, and M.Th. van Genuchten. 2015. Evaluation of a horizontal permeable reactive barrier for preventing upward diffusion of volatile organic compounds

through the unsaturated zone. J. Environ. Manage. 163:204–213. doi:10.1016/j.jenvman.2015.08.025

Masís-Meléndez, F., L.W. de Jonge, T.K.K. Chamindu Deepagoda, M. Tuller, and P. Moldrup. 2015. Effects of soil bulk density on gas transport parameters and pore-network properties across a sandy field site. Vadose Zone J. 14(7). doi:10.2136/vzj2014.09.0128

Matthews, G.P., G.M. Laudone, A.S. Gregory, N.R.A. Bird, A.G. Matthews, and W.R. Whalley. 2010. Measurement and simulation of the effect of compaction on the pore structure and saturated hydraulic conductivity of grassland and arable soil. Water Resour. Res. 46:W05501. doi:10.1029/2009WR007720

Mehlhorn, T., S. Prohaska, U. Homberg, and V. Slowik. 2008. Modelling and analysis of particle and pore structures in soils. In: K.J. Witt, editor, Workshop Internal Erosion. 26–28 Nov. 2008. Schriftenreihe Geotechnik 21. Bauhaus-Universität, Weimar, Germany. p. 53–60.

Mousavi, M.A., and S.L. Bryant. 2012. Connectivity of pore space as a control on two-phase flow properties of tight-gas sandstones. Transp. Porous Media 94:537–554. doi:10.1007/s11242-012-0017-x

Øren, P., S. Bakke, and O.J. Arntzen. 1998. Extending predictive capabilities to network models. Soc. Pet. Eng. J. 3:324–336.

Peth, S., J. Nellesen, G. Fischer, and R. Horn. 2010. Non-invasive 3D analysis of local soil deformation under mechanical and hydraulic stresses by mCT and digital image correlation. Soil Tillage Res. 111:3–18. doi:10.1016/j.still.2010.02.007

Prodanović, M., A. Mehmani, and A.P. Sheppard. 2015. Imaged-based multiscale network modelling of microporosity in carbonates. Geol. Soc. London Spec. Publ. 406:95–113. doi:10.1144/SP406.9

Rajkai, K., S. Kabos, M.Th. van Genuchten, and P.E. Jansson. 1996. Estimation of water retention characteristics from bulk density and particle distribution of Swedish soils. Soil Sci. 161:832–845. doi:10.1097/00010694-199612000-00003

Raoof, A., and S.M. Hassanizadeh. 2010. A new method for generating pore-network models of porous media. Transp. Porous Media 81:391–407. doi:10.1007/s11242-009-9412-3

Raoof, A., and S.M. Hassanizadeh. 2012. A new formulation for pore-network modeling of two-phase flow. Water Resour. Res. 48:W01514. doi:10.1029/2010WR010180

Raoof, A., S.M. Hassanizadeh, and A. Leijnse. 2010. Upscaling transport of adsorbing solutes in porous media: Pore-network modeling. Vadose Zone J. 9:624–636. doi:10.2136/vzj2010.0026

Raoof, A., H.M. Nick, S.M. Hassanizadeh, and C.J. Spiers. 2013. PoreFlow: A complex pore-network model for simulation of reactive transport in variably saturated porous media. Comput. Geosci. 61:160–174. doi:10.1016/j.cageo.2013.08.005

Rawls, W.J., D.L. Brakensiek, and B. Soni. 1983. Agricultural management effects on soil water processes: I. Soil water retention and Green and Ampt infiltration parameters. Trans. ASAE 26:1747–1752. doi:10.13031/2013.33837

Richard, G., I. Cousin, J.F. Sillon, A. Bruand, and J. Guérif. 2001a. Effect of compaction on the porosity of a silty soil: Influence on unsaturated hydraulic properties. Eur. J. Soil Sci. 52:49–58. doi:10.1046/j.1365-2389.2001.00357.x

Richard, G., J.F. Sillon, and O. Marloie. 2001b. Comparison of inverse and direct evaporation methods for estimating soil hydraulic properties under different tillage practices. Soil Sci. Soc. Am. J. 65:215–224. doi:10.2136/sssaj2001.651215x

Scholtès, L., and F.V. Donzé. 2012. Modelling progressive failure of fractured rock masses using a 3D discrete element method. Int. J. Rock Mech. Min. Sci. 52:18–30. doi:10.1016/j.ijrmms.2012.02.009

Scholtès, L., P.Y. Hicher, F. Nicot, B. Chareyre, and F. Darve. 2009. On the capillary stress tensor in wet granular materials. Int. J. Numer. Anal. Methods Geomech. 33:1289–1313. doi:10.1002/nag.767

Sela, S., T. Svoray, and S. Assouline. 2015. The effect of soil surface sealing on vegetation water uptake along a dry climatic gradient. Water Resour. Res. 51:7452–7466. doi:10.1002/2015WR017109

Shmulevich, I., Z. Asaf, and D. Rubinstein. 2007. Interaction between soil and a wide cutting blade using the discrete element method. Soil Tillage Res. 97:37–50. doi:10.1016/j.still.2007.08.009

Šmilauer, V., E. Catalano, B. Chareyre, S. Dorofeenko, J. Duriez, A. Gladky, et al. 2015. Yade documentation. 2nd ed. The Yade Project, Grenoble, France. doi:10.5281/zenodo.34073

Stange, C.F., and R. Horn. 2005. Modeling the soil water retention curve for conditions of variable porosity. Vadose Zone J. 4:602–613. doi:10.2136/vzj2004.0150

Sweijen, T., E. Nikooee, S.M. Hassanizadeh, and B. Chareyre. 2016. The effects of swelling and porosity change on capillarity: DEM coupled with a pore unit assembly method. Transp. Porous Media 113:207–226. doi:10.1007/s11242-016-0689-8

Tong, A.T., E. Catalano, and B. Chareyre. 2012. Pore-scale flow simulations: Model predictions compared with experiments on bi-dispersed granular assemblies. Oil Gas Sci. Technol. 67:743–752. doi:10.2516/ogst/2012032

Torskaya, T., V. Shabro, C. Torres-Verdín, R. Salazar-Tio, and A. Revil. 2014. Grain shape effects on permeability, formation factor, and capillary pressure from pore-scale modeling. Transp. Porous Media 102:71–90. doi:10.1007/s11242-013-0262-7

Unsal, E., G. Mason, N.R. Morrow, and D.W. Ruth. 2009. Bubble snap-off and capillary-back pressure during counter-current spontaneous imbibition into model pores. Langmuir 25:3387–3395. doi:10.1021/la803568a

Vahyala I.E., A.I. Zata, G.A. Adediron, I.S. Dzarma. 2013. Impacts of compaction on selected physical properties of tropical soils at Yola, Nigeria. Adv. Agric. Res. Dev. 1(1):9–15.

van Genuchten, M.Th. 1980. A closed-form equation for predicting the hydraulic conductivity of unsaturated soils. Soil Sci. Soc. Am. J. 44:892–898. doi:10.2136/sssaj1980.03615995004400050002x

van Genuchten, M.Th., F.J. Leij, and S.R. Yates. 1991. The RETC code for quantifying the hydraulic functions of unsaturated soils. EPA/600/2-91/065. USEPA, R.S. Kerr Environ. Res. Lab., Ada, OK.

Vasilyev, L., A. Raoof, and J.M. Nordbotten. 2012. Effect of mean network coordination number on dispersivity characteristics. Transp. Porous Media 95:447–463. doi:10.1007/s11242-012-0054-5

Vaz, C.M.P., M. Tuller, P.R.O. Lasso, and S. Crestana. 2014. New perspectives for the application of high-resolution benchtop X-ray microCT for quantifying void, solid and liquid phases in soils. In: W.G. Teixeira et al., editors, Application of soil physics in environmental analyses: Measuring, modelling and data integration. Progr. Soil Sci. Springer Int. Publ., Cham, Switzerland. p. 261–281. doi:10.1007/978-3-319-06013-2_12

Wall, A., and J. Heiskanen. 2009. Soil-water content and air-filled porosity affect height growth of Scots pine in afforested arable land in Finland. For. Ecol. Manage. 257:1751–1756. doi:10.1016/j.foreco.2009.01.029

Xu, Y., K.D. Kafui, C. Thornton, and G. Lian. 2002. Effects of material properties on granular flow in a silo using DEM simulation. Part. Sci. Technol. 20:109–124. doi:10.1080/02726350215338

Yuan, C., B. Chareyre, and F. Darve. 2015. Pore-scale simulations of drainage in granular materials: Finite size effects and the representative elementary volume. Adv. Water Resour. (in press). doi:10.1016/j.advwatres.2015.11.018

Zhang, Q., S.M. Hassanizadeh, N.K. Karadimitriou, A. Raoof, B. Liu, P.J. Kleingeld, and A. Imhof. 2013. Retention and remobilization of colloids during steady-state and transient two-phase flow. Water Resour. Res. 49:8005–8016. doi:10.1002/2013WR014345

Zhang, Q., A. Raoof, and S.M. Hassanizadeh. 2015. Pore-scale study of flow rate on colloid attachment and remobilization in a saturated micromodel. J. Environ. Qual. 44:1376–1383. doi:10.2134/jeq2015.01.0058